

Heat Transfer Engineering



Date: 05 July 2017, At: 07:13

ISSN: 0145-7632 (Print) 1521-0537 (Online) Journal homepage: http://www.tandfonline.com/loi/uhte20

Effect of Buoyancy Ratio on Double-Diffusive Natural Convection in a Porous Rhombic Annulus

Fadl Moukalled & Marwan Darwish

To cite this article: Fadl Moukalled & Marwan Darwish (2015) Effect of Buoyancy Ratio on Double-Diffusive Natural Convection in a Porous Rhombic Annulus, Heat Transfer Engineering, 36:16, 1371-1386, DOI: 10.1080/01457632.2015.1003716

To link to this article: http://dx.doi.org/10.1080/01457632.2015.1003716

	Accepted author version posted online: 12 Jan 2015. Published online: 12 Jan 2015.
	Submit your article to this journal ${\it \mathbb{G}}$
lılı	Article views: 99
Q	View related articles ☑
CrossMark	View Crossmark data ☑
4	Citing articles: 1 View citing articles 🗹

Full Terms & Conditions of access and use can be found at http://www.tandfonline.com/action/journalInformation?journalCode=uhte20

Heat Transfer Engineering, 36(16):1371-1386, 2015 Copyright © Taylor and Francis Group, LLC ISSN: 0145-7632 print / 1521-0537 online DOI: 10.1080/01457632.2015.1003716



Effect of Buoyancy Ratio on Double-Diffusive Natural Convection in a Porous Rhombic Annulus

FADL MOUKALLED and MARWAN DARWISH

Department of Mechanical Engineering, American University of Beirut, Beirut, Lebanon

This paper reports on the effect of buoyancy ratio due to both heat and mass transfer on natural convection in a porous enclosure between two isothermal concentric cylinders of rhombic cross sections. For negative values of the buoyancy ratio, buoyancy forces due to heat and mass transfer are in opposite directions (opposing mode), while for positive values they are in the same direction (aiding mode). Numerical results demonstrate that the flow strength increases as the absolute value of the buoyancy ratio increases. In the opposing mode, the eye of the vortex flow is located in the lower half of the enclosure, while in the aiding mode it is positioned in the upper part of the annulus. The average Nusselt and Sherwood number values increase as the absolute value of the buoyancy ratio moves away from 1, with values obtained in the aiding mode being higher than corresponding values achieved in the opposing mode. A comparison is also made between the computed average Nusselt and Sherwood number values and similar ones obtained in a circular annulus having the same inner and outer perimeters as the rhombic enclosure. Predictions indicate large percent difference in values, demonstrating that circular geometries cannot be exploited to accurately predict heat and mass transfer in complex geometries.

INTRODUCTION

Natural convection flows in porous enclosures resulting from the combined buoyancy effects of temperature and concentration nonuniformity are still attracting attention due to their appearance in a wide range of industrial applications such as migration of moisture in fibrous insulation, the growth of crystals, food processing, and solar energy systems, to cite a few [1–4]. In a recent article, Moukalled and Darwish [5] analyzed the effects of Rayleigh number, Darcy number, porosity, enclosure gap, and Prandtl number on double-diffusive natural convection heat transfer in a porous annulus between two horizontal pipes of rhombic cross section. The intention of this paper is to extend the work reported in [5] and to study the effect of the buoyancy ratio (the buoyancy due to concentration gradient to that resulting from temperature gradient) on the hydrodynamic, thermal, and mass transfer fields in the same geometry.

Address correspondence to Professor Fadl Moukalled, Department of Mechanical Engineering, American University of Beirut, PO Box 11-0236, Riad El Solh, Beirut 1107 2020, Lebanon. E-mail: fmukalled@aub.edu.lb

Extensive work on double-diffusive natural convection in square and rectangular enclosures appears in the literature. Nithiarasu et al. [6] reported on double-diffusive natural convection in a rectangular enclosure using a generalized porous medium approach covering the entire range from Darcy flow to free fluid flow. Borjini et al. [7] studied numerically the twodimensional hydromagnetic double-diffusive convection of a radiatively participating fluid confined in a rectangular enclosure with uniform temperatures and concentrations imposed along the vertical walls, while the horizontal walls were assumed to be adiabatic and impermeable. Nishimura et al. [8] analyzed the mechanism of layer merging in a salt-stratified system by solving numerically unsteady double-diffusive convection in a rectangular enclosure using the Chebyshev collocation method. Mansour et al. [9] studied numerically the Soret effect on fluid flow and heat and mass transfer induced by double-diffusive natural convection in a square porous enclosure, subjected to cross gradients of temperature and concentration. Ghorayeb et al. [10] reported on unsteady double-diffusive convection in a square cavity with equal but opposing horizontal temperature and concentration gradients. Their numerical results indicated that steady-state convective flow is stable up to a threshold value of the thermal Grashof number, which depends on the Lewis number. Wang et al. [11] analyzed experimentally, using particle image velocimetry (PIV), double-diffusive convection of a binary NH₄Cl-H₂O solution in a rectangular enclosure during solidification. The double-diffusive flow was found to be stronger at the beginning of solidification with the flow decaying as solidification proceeded. Costa [12] studied numerically steady double-diffusive natural convection in a vertical stack of square enclosures. Chen and Liou [13] investigated the time-dependent double-diffusive convection of NaCl-H2O stably stratified salt fluid layer with lateral heating in an inclined cavity. Li et al. [14] investigated numerically small-scale phenomena in double-diffusive convection flows at high Rayleigh number. Their quasi-steady predictions agreed well with experimental data and indicated that the flow pattern is scattered with abundant salt fingers and hook-like plumes. Tanny and Yakubov [15] carried out an experimental study to investigate the mixing process of a two-layer stratified fluid in a laterally heated enclosure. Their results showed that when the flow adjacent to the interface is unstable, it is characterized by intense vortices and the mixing time is relatively short. On the other hand, when the interfacial flow is stable, no vortices exist at the interface and the mixing time is much longer. Tanny et al. [16] conducted experiments to investigate the structure of a double-diffusive interface separating two layers in a laterally heated enclosure.

Several studies dealing with double-diffusive natural convection heat transfer in cylindrical enclosures have also been reported. Lee et al. [17] investigated numerically, using a finite-difference method, the flow and heat transfer characteristics of a salt—water solution in a rotating annulus subjected to lateral heating. Shi and Lu [18] simulated numerically using a finite-element method the time evolution of double-diffusive convection in a vertical cylinder to identify the effect of the buoyancy ratio on the evolution of the flow, temperature, and solute fields in the cavity. Lee et al. [19] conducted an experimental investigation to study the double-diffusive convection phenomena of a stably stratified salt—water solution due to lateral heating in a stationary and rotating annulus. In the stationary annulus, four distinct flow regimes were observed. In the rotating annulus, only a fully formed layer flow regime was observed.

A number of studies on double-diffusive natural convection in porous enclosures have also appeared in the literature. Kumar et al. [20] conducted a numerical study, using the Galerkin finite-element method, on combined heat and mass transfer by natural convection in a porous enclosure. Saghir and Islam [21] performed a numerical study, using a finite-element formulation for a wide range of permeability contrasts, of double-diffusive phenomena in porous media. Malashetty and Basavaraja [22] used the perturbation method to study the effect of time-periodic boundary temperatures on the onset of double-diffusive convection in a fluid-saturated anisotropic porous medium. Chamkha [23] reported on unsteady, laminar double-diffusive convective flow of a binary gas mixture in a rectangular enclosure filled with a uniform porous medium subject to a temperature-dependent heat source or sink. Capone et al. [24] explored

double-diffusive convection in an anisotropic porous layer with a constant throughflow. Karimi-Fard et al. [25] studied numerically, using the finite-volume method, the effect of Darcy and Lewis number on double-diffusive natural convection in a square cavity filled with a porous medium. Their study revealed that the inertial and boundary effects have a profound influence on the double-diffusive convection. Bennacer et al. [26] presented a study on double-diffusive natural convection in a square cavity filled with porous media heated and cooled along vertical walls by uniform heat fluxes when a solutal flux is imposed vertically. Bera and Khalili [27] studied double-diffusive natural convection in an anisotropic porous cavity with the principal directions of the permeability tensor taken oblique to the gravity vector, with those of thermal and solutal diffusivity coinciding with horizontal and vertical coordinate axes. Beji et al. [28] carried out a numerical investigation to study the combined effects of thermal and solutal buoyancy forces on the flow, heat, and mass transfer in a vertical annular porous layer subjected to constant temperature and concentration boundary conditions. Costa [29, 30] predicted numerically double-diffusive natural convection in parallelogrammic enclosures filled with fluid-saturated porous media. Results showed the strong potential of this configuration for heat and mass transfer applications.

Recently, Moukalled and Darwish [5, 31] reported on the natural convection heat transfer in a porous annulus between two horizontal pipes of rhombic cross section [31] and then analyzed the effects of Rayleigh number, Darcy number, porosity, enclosure gap, and Prandtl number on double-diffusive natural convection heat transfer in the same enclosure [5]. As buoyancy ratio is the primary factor that defines the flow structure, it is the intention of this paper to extend the work reported in [5] and to study the effect of the buoyancy ratio on the hydrodynamic, thermal, and mass transfer fields in the same geometry. Another objective of the paper is to compare the predicted rates of heat and mass transfer with similar ones obtained in a circular annulus of the same inner and outer perimeters as the rhombic enclosure.

PHYSICAL MODEL AND GOVERNING EQUATIONS

The physical situation under consideration is shown schematically in Figure 1a. Numerical solutions for double-diffusive natural convection in the right side of the rhombic annulus are obtained for the case when the inner enclosure walls are maintained at the uniform hot temperature and high concentration T_h and S_h , respectively, and the outer walls are maintained at the uniform cold temperature and low concentration T_c and S_c , respectively. In the configuration studied, the length of the main diagonal of the inner pipe is D_i , while that of the outer pipe is D_o . The enclosure is assumed to be filled with a porous material of porosity ϵ . The flow established in the cavity, caused by buoyancy forces resulting from temperature and concentration gradients, is assumed to be steady, incompressible, and

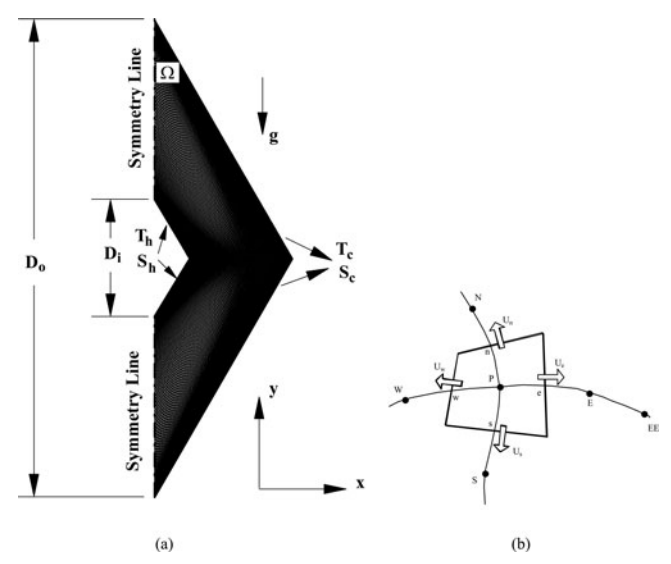


Figure 1 (a) Computational domain showing a grid network and (b) a typical control volume.

two-dimensional. The problem is solved assuming local thermal equilibrium between the fluid and the porous matrix, while retaining the non-Darcian terms in the conservation equations [32–34].

Employing the Boussinesq approximation given by

$$\rho = \rho_{\infty} \left[1 - \beta_T \left(T - T_{\infty} \right) - \beta_S \left(S - S_{\infty} \right) \right] \tag{1}$$

where

$$\beta_T = -\frac{1}{\rho} \left(\frac{\partial \rho}{\partial T} \right)_{p,S} \text{ and } \beta_S = -\frac{1}{\rho} \left(\frac{\partial \rho}{\partial S} \right)_{p,T}$$

and defining the following dimensionless variables

$$X = \frac{x}{D_o}, \ Y = \frac{y}{D_o}, \ U = \frac{u}{\sqrt{g\beta_T (T_h - T_c) D_o}},$$
$$V = \frac{v}{\sqrt{g\beta_T (T_h - T_c) D_o}}, \Pr = \frac{\mu c_p}{k}, \tag{3}$$

$$P = \frac{p + \rho g y}{\rho g \beta_T (T_h - T_c) D_o}, \ \theta = \frac{T - T_c}{T_h - T_c},$$

$$Ra_T = \frac{\rho g \beta_T (T_h - T_c) D_o^3}{\mu \alpha}, \ \sigma = \frac{S - S_c}{S_h - S_c},$$
 (4)

$$Ra_S = \frac{\rho g \beta_S \left(S_h - S_c\right) D_o^3}{\mu \alpha}, \ Le = \frac{\alpha}{D}, \ Da = \frac{K}{D_o^2},$$

$$F = \frac{1.75}{\sqrt{150\epsilon^3}}, \ K = \frac{\epsilon^3 d_p^2}{150(1-\epsilon)^2}, \ N = \frac{Ra_S}{Ra_T}$$
 (5)

the nondimensional volume-averaged equations [35] governing conservation of mass, momentum, energy, and concentration are

heat transfer engineering

respectively written as

$$\frac{\partial U}{\partial X} + \frac{\partial V}{\partial Y} = 0. ag{6}$$

$$\frac{1}{\varepsilon^2} \left(U \frac{\partial U}{\partial X} + V \frac{\partial U}{\partial Y} \right) = \frac{1}{\varepsilon} \sqrt{\frac{\Pr}{Ra_T}} \left(\frac{\partial^2 U}{\partial X^2} + \frac{\partial^2 U}{\partial Y^2} \right) - \frac{\partial P}{\partial X}$$

$$-\frac{1}{Da}\sqrt{\frac{\Pr}{Ra_T}}U - \frac{F}{\sqrt{Da}}\left(U^2 + V^2\right)^{1/2}U \tag{7}$$

$$\frac{1}{\varepsilon^2} \left(U \frac{\partial V}{\partial X} + V \frac{\partial V}{\partial Y} \right) = \frac{1}{\varepsilon} \sqrt{\frac{\Pr}{Ra_T}} \left(\frac{\partial^2 V}{\partial X^2} + \frac{\partial^2 V}{\partial Y^2} \right) - \frac{\partial P}{\partial Y}$$

$$-\frac{1}{Da}\sqrt{\frac{\Pr}{Ra_{T}}}V - \frac{F}{\sqrt{Da}}(U^{2} + V^{2})^{1/2}V + (\theta + N\sigma)$$
 (8)

$$U\frac{\partial\theta}{\partial X} + V\frac{\partial\theta}{\partial Y} = \frac{1}{\sqrt{Ra_T \Pr}} \left(\frac{\partial^2\theta}{\partial X^2} + \frac{\partial^2\theta}{\partial Y^2} \right)$$
(9)

$$U\frac{\partial \sigma}{\partial X} + V\frac{\partial \sigma}{\partial Y} = \frac{1}{Le\sqrt{Ra_T \Pr}} \left(\frac{\partial^2 \sigma}{\partial X^2} + \frac{\partial^2 \sigma}{\partial Y^2} \right)$$
(10)

The meanings of the various dimensionless numbers are given in the Nomenclature list at the end of this paper. In specific, the parameter N appearing in Eq. (8) is the buoyancy ratio, which is the subject of the current study. It is the ratio between the solute and thermal buoyancy forces and can be either positive or negative, depending on the sign of the concentration volumetric expansion coefficient β_S . For positive values of N, the temperature and concentration buoyancy effects are combined (aiding mode), while for negative values they are opposite (opposing mode).

The boundary conditions used are

$$U = \frac{\partial V}{\partial X} = \frac{\partial \theta}{\partial X} = \frac{\partial \sigma}{\partial X} = 0 \text{ along symmetry lines} \quad (11)$$

$$U = V = 0, \ \theta = \sigma = 1$$
 at inner walls (12)

$$U = V = \theta = \sigma = 0$$
 at outer walls (13)

The results for the flow field are displayed via streamlines calculated using the following definition of the steam function:

$$\frac{1}{\varepsilon^2}U = \frac{\partial \psi}{\partial Y}$$
 and $\frac{1}{\varepsilon^2}V = -\frac{\partial \psi}{\partial X}$ (14)

Moreover, heat and mass transfer results are reported in terms of local Nusselt (Nu) and Sherwood (Sh) number values calculated as

$$Nu_i = -\frac{D_i}{D} \nabla \theta_i \cdot \mathbf{n} \quad Nu_o = -\nabla \theta_o \cdot \mathbf{n}$$

$$Sh_i = -\frac{D_i}{D_o} \nabla S_i \cdot \mathbf{n} \quad Sh_o = -\nabla S_o \cdot \mathbf{n}$$
 (15)

and by means of average Nusselt (\overline{Nu}) and Sherwood (\overline{Sh}) number estimates computed using

$$\overline{Nu} = \overline{Nu}_{i/o} = \frac{1}{A_{i/o}} \int_{i/o} Nu_{i/o} ds$$

$$\overline{Sh} = \overline{Sh}_{i/o} = \frac{1}{A_{i/o}} \int_{i/o} Sh_{i/o} ds$$
(16)

SOLUTION PROCEDURE

The problem is solved numerically using a finite-volume method. In this approach, the domain is subdivided into a number of control volumes (Figure 1a) with grid points placed at their geometric centers. The conservation equations [Eqs. (6) to (10)] are integrated over each control volume and transformed into algebraic equations. The diffusion flux is discretized using the method described in Zwart et al. [36], while the convective flux at the control volume faces is evaluated using the pseudothird-order SMART scheme [37], applied within the context of the NVSF methodology [38]. Moreover, a second-order scheme is used to calculate the value of the source term over a control volume (Figure 1b). The resulting system of algebraic equations is then solved by a block-Thomas algorithm [39]. A pressurebased method is used and the pressure field is computed by defining a pressure correction field $p' (= p - p^*)$, where p^* is the solution from the previous iteration) and deriving a pressure correction equation as in the SIMPLE procedure of Patankar [39–41]. Finally, a collocated grid is adopted and checkerboard pressure and velocity fields are suppressed through the use of the momentum weighted interpolation method (MWIM) [42].

Numerical Accuracy and Validation

All grid-independent results reported in this paper are generated using a nonuniform grid (Figure 1a) with a size of 160×128 control volumes. The grid size was selected after comparing the solutions obtained using several grid systems of increasing density [5]. The comparison of solutions for some of the cases with similar ones obtained on a grid with a size of 240×240 control volumes revealed that the maximum differences in the average Nusselt and Sherwood number values were less than 0.0156%. Conservation of the various physical quantities was satisfied to within 10^{-8} for each control volume.

The correctness of the solution procedure already described is established by comparing results obtained from the present model with corresponding results reported in the literature for double-diffusive natural convection in a square [25] and a parallelogrammic enclosure [29]. For the square enclosure, computed average Nusselt and Sherwood number values (N = 0, Le = 10, and Ra_T = 100 and 200) are compared in Table 1 with values reported by several workers [25, 43, 44]. The percent differences between the predicted average Nusselt and Sherwood number values and values reported in reference 43 are 0.19%

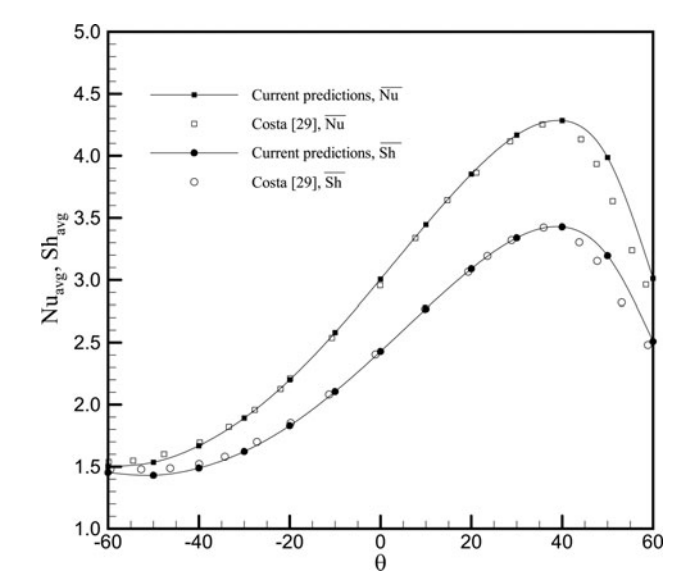


Figure 2 Comparison of predicted average Nusselt and Sherwood number in a parallelogrammic enclosure with similar ones reported by Costa [29].

and -0.973% at Ra_T = 100 and 0.12% and -1.62% at Ra_T = 200, respectively. For the parallelogrammic enclosure problem, the computed average Nusselt and Sherwood number values (for N = 2, Le = 0.8, and Ra_T = 25) are compared in Figure 2 with similar ones reported by Costa [29]. As explained in reference 5, reported and predicted \overline{Nu} and \overline{Sh} values are in good agreement, with the maximum difference being lower than 3%, confirming the correctness of the developed solution procedure.

RESULTS AND DISCUSSION

The geometric parameters affecting the natural convection heat transfer in this study are the enclosure gap ($E_g = 1$ – D_i/D_o), which is assigned three different values (E_g = 0.875, 0.75, and 0.5), and the rhombus angle (Ω), which is fixed at 30° . On the other hand, the thermophysical parameters in the problem are the porosity (ε), the thermal Rayleigh number (Ra_T), the Prandtl number (Pr), the Darcy number (Da), the buoyancy ratio ($N = Ra_S/Ra_T$), and the Lewis number (Le). Air and water are considered to be the working fluids and, as such, the Prandtl number is assigned the two values of 0.7 and 5 while the Lewis number is fixed at 10. Moreover, three different values of thermal Rayleigh number ($Ra_T = 10^5$, 10^6 , and 10^7), two different values of Darcy number (Da = 10^{-3} and 10^{-5}), three different values of porosity ($\varepsilon = 0.3, 0.6,$ and 0.9), and six different values of buoyancy ratio (N = -100, -10, -1, 1, 10, and 100)are considered. The diffusion of trimethybenzene (treated as a solute) in air at a pressure of 3.2 atm and a temperature of 25°C results in a situation for which the value of Lewis number is 10. Moreover, the diffusion of hydrogen in water may be considered a good representation of the case for which water is the solvent (i.e., Pr = 5).

Results are presented in the form of streamlines, isotherms, isoconcentrations, mid-height velocity, temperature, and con-

heat transfer engineering

Table 1 Comparison of current average Nusselt and Sherwood number results in a square enclosure (Le = 10, N = 0) with similar ones reported by Karimi-Fard et al. [25], Goyeau et al. [43], and Trevisan and Bejan [44]

		Ra _T :	= 100			Ra _T :	= 200	
	Present work	Ref. [25]	Ref. [43]	Ref. [44]	Present work	Ref. [25]	Ref. [43]	Ref. [44]
$\frac{\overline{Nu}}{\overline{Sh}}$	3.104 13.379	3.11 13.43	3.11 13.25	3.27 15.61	4.954 20.182	4.97 20.32	4.96 19.86	5.61 23.23

centration profiles, and local and average Nusselt and Sherwood number values. However, prior to discussing results, the issues of flow symmetry and flow steadiness are first addressed.

Flow Symmetry

In the mathematical model, natural convection does not always maintain the symmetry of the flow even in a symmetrical configuration. Therefore, to be able to apply the symmetry mathematically and perform computations in only half of the domain, symmetry of the flow for the configuration considered should be established. For that purpose, computations for $Ra_T=10^5,\,10^6,\,$ and 10^7 are performed over an entire rhombic annulus using the parameters in the study that are expected to result in the strongest flow (i.e., $E_g=0.875,\, \epsilon=0.9,\, Pr=5,\, Le=10,\, N=100,\, Da=10^{-3}$). Generated solutions are displayed in Figures 3a–3i. As can be seen, for all Rayleigh number values, streamlines (Figures 3a–3c), isotherms (Figures 3d–3f), and isoconcentrations (Figures 3g–3i), are fully symmetric, justifying obtaining solutions in only half of the domain while applying the symmetry boundary condition.

Flow Steadiness

Steady-state solutions are of interest in this study and are obtained using an iterative approach. Since some of the Ra_T and N values are too large, a confirmation that a steady solution exists is required. For that purpose, the same cases considered to establish flow symmetry are solved here, over only half the domain, but via a time-marching approach. The intention is not to obtain accurate predictions in time, but rather to check whether a steady-state solution for each case exists. Computations are performed, and results demonstrating the variations of the average Nusselt and Sherwood numbers along the cold and hot walls of the rhombic enclosure as a function of time for the three cases considered are plotted in Figures 4a–4d. Figures 4a and 4b display the average Nusselt number values along the cold and hot walls of the annulus, respectively, while Figures 4c and 4d report the variations of the Sherwood number. Computations are extended over a long period of time and, as seen, the values of all quantities and for all Ra_T considered vary over a certain period of time, reaching a certain level and remaining constant afterward, confirming that steady-state solutions exist.

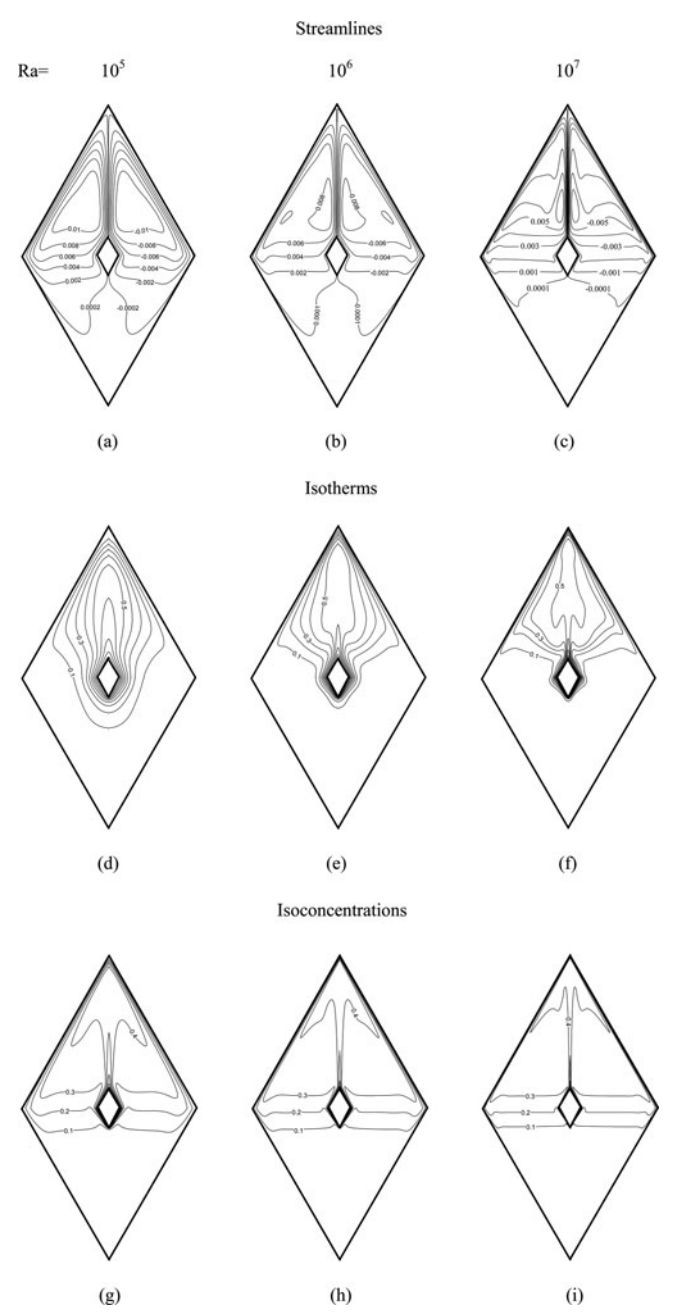


Figure 3 Streamlines, isotherms, and isoconcentrations for different values of Rayleigh number (Ra) obtained over the entire rhombic annulus ($E_g=0.875$, $\epsilon=0.9$, $P_g=5$, $P_g=5$, $P_g=10$, $P_g=100$, $P_$

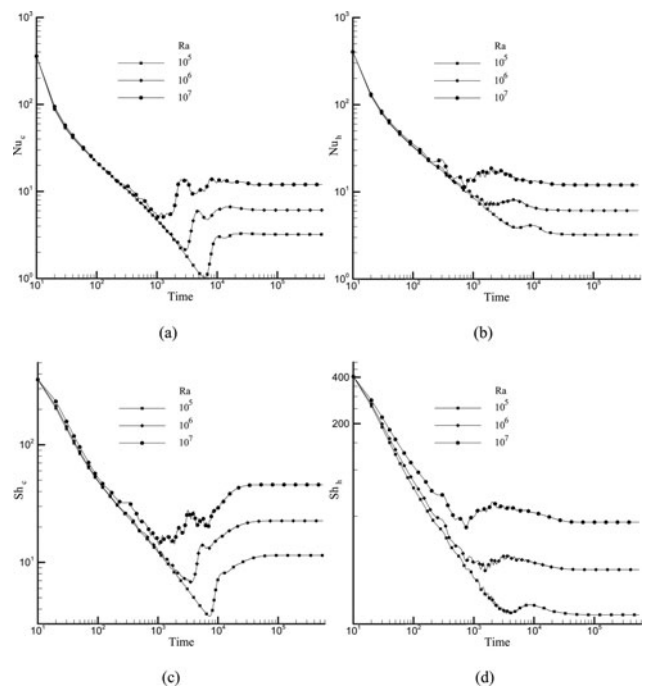


Figure 4 Variations with time of average Nusselt (a,b) and Sherwood (c,d) numbers along the cold (a,c) and hot (b,d) walls of a rhombic annulus as steady state is reached for different values of Rayleigh number ($E_g=0.875,\,\epsilon=0.9,\,Pr=5,\,Le=10,\,N=100,\,Da=10^{-3}$).

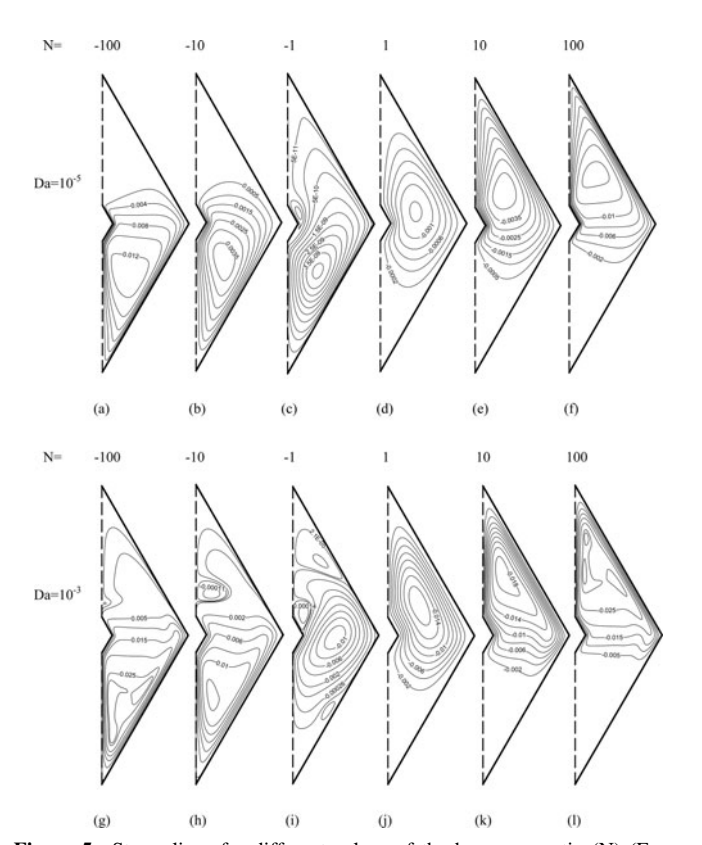


Figure 5 Streamlines for different values of the buoyancy ratio (N) ($E_g = 0.875, \epsilon = 0.6, Ra = 10^6, Pr = 0.7$).

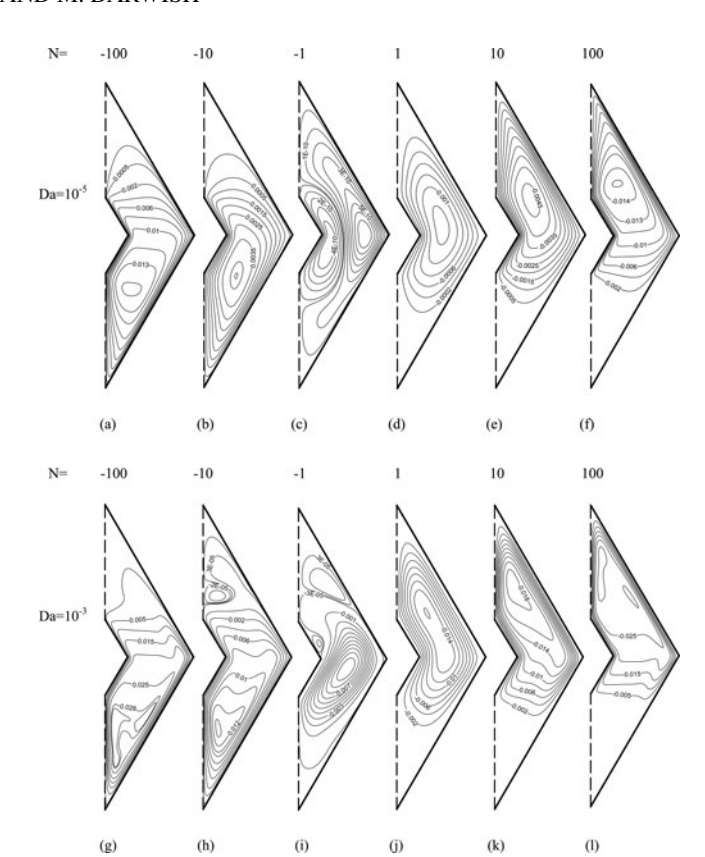


Figure 6 Streamlines for different values of the buoyancy ratio (N) (Eg = 0.75, ϵ = 0.6, Ra = 10^6 , Pr = 0.7).

Streamlines, Isotherms, and Isoconcentrations

The effects of the buoyancy ratio on the flow, temperature, and concentration fields are revealed by the streamlines, isotherms, and isoconcentrations depicted in Figures 5 through 10 in an enclosure with $\epsilon=0.6$, $Ra_T=10^6$, and Pr=0.7. Figures 5, 7, and 9 are for an annulus with a value of $E_g=0.875$, while Figures 6, 8, and 10 are for a value of $E_g=0.75$. In all figures, plots for the various values of the buoyancy ratio are presented for the two values of Da considered in this study (i.e., $Da=10^{-5}$ and 10^{-3}). Streamlines are displayed in Figures 5 and 6, isotherms in Figures 7 and 8, and isoconcentrations in Figures 9 and 10.

Before discussing results, it should be clarified that the streamlines for N=-1 can be very different depending on the numerical code and the minimum residuals considered, as the fluid is essentially stagnant for this value of buoyancy ratio. Their inclusion as part of the results is for completeness of presentation.

Streamlines depicted in Figures 5 and 6 indicate that the dominant feature of the flow is a recirculating eddy rotating generally counterclockwise for negative values of the buoyancy ratio and clockwise for positives values of N. The eye of the vortex is located in the lower part of the domain for negative values of N and in the upper part of the enclosure for positive values of N. The eye moves further downward and toward the

heat transfer engineering

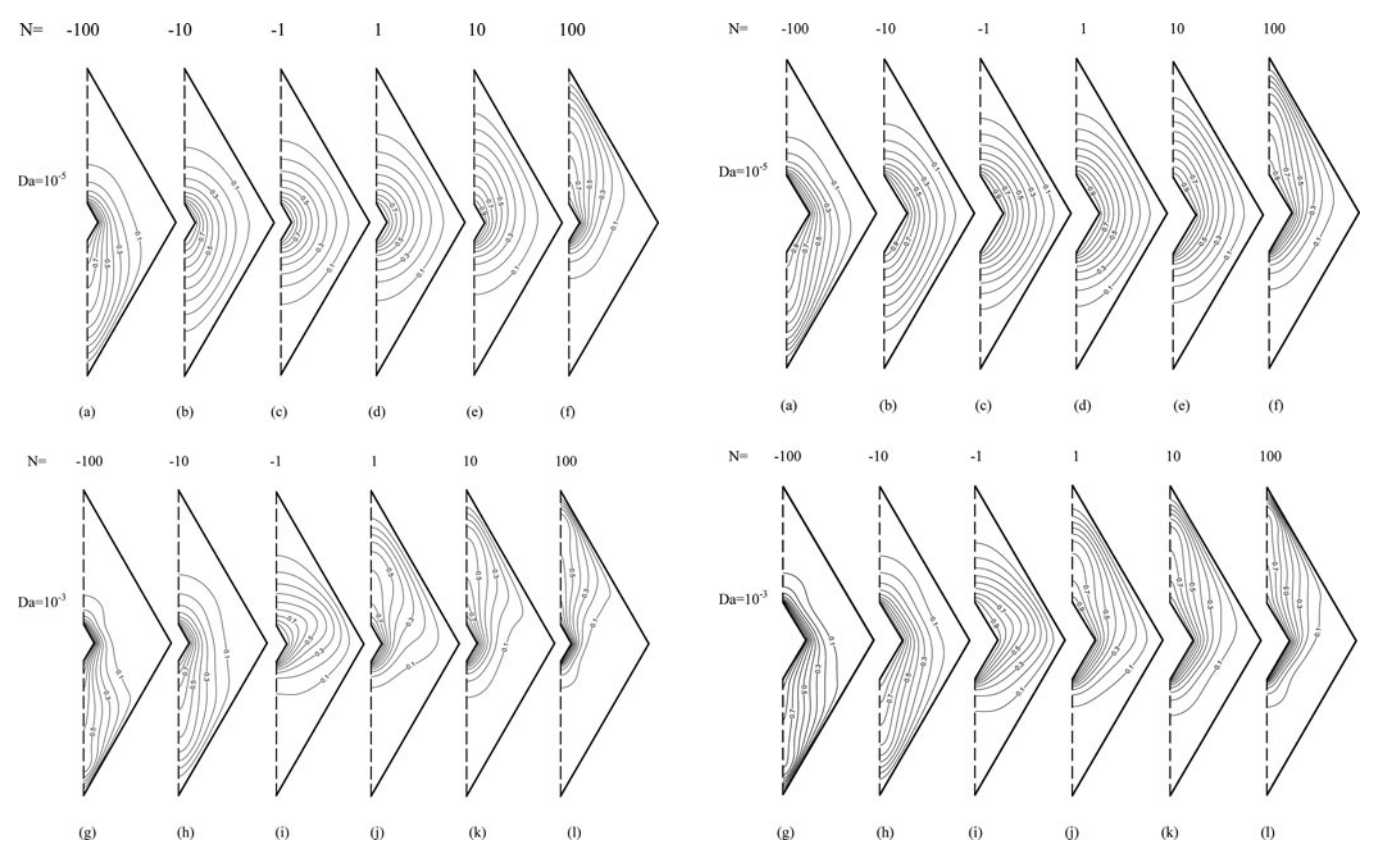


Figure 7 Isotherms for different values of the buoyancy ratio (N) ($E_g = 0.875$, $\epsilon = 0.6$, $Ra = 10^6$, Pr = 0.7).

Figure 8 Isotherms for different values of the buoyancy ratio (N) (E $_g=0.75,\,\epsilon=0.6,\,Ra=10^6,\,Pr=0.7).$

symmetry line as the downward buoyancy ratio increases (i.e., N < 0) and further upward and toward the symmetry line as the upward buoyancy ratio increases (i.e., N > 0). For negative values of N the concentration gradients give rise to a downward buoyant force while the temperature gradients create an upward buoyant force. The resultant of these two opposite forces is the driving power that dictates the direction of rotation and characteristics of the flow field. Moreover, results in Figures 5 and 6 indicate that the flow is stronger at higher value of Da $(Da = 10^{-3})$ due to a higher permeability of the porous medium $(Da = K/D_0^2)$ and its strength increases as |N| moves away from 1, in either direction, due to higher buoyancy forces.

For $E_g=0.875$ and $Da=10^{-5}$, the flow at N=-100 and -10 (Figures 5a and 5b) is confined to the lower portion of the domain with a highly stratified region formed in the upper part where the flow is practically stagnant. As N increases to -1, the effects of the downward buoyancy forces created by concentration gradients are counterbalanced by the upward buoyancy forces arising from temperature gradients. As a result, the flow within the enclosure is very weak (Figure 5c) and a bubble rotating clockwise is formed close to the upper hot wall. For positive values of N, buoyancy forces due to concentration and temperature gradients are in the aiding mode, resulting in the flow fields presented in Figures 5d through 5f. The flow at N=1 is nearly symmetrical with respect to the horizontal centerline of the cavity. As N increases to 10 (Figure 5e) and

then 100 (Figure 5f) the flow strength increases and stratification in the lower part of the enclosure increases with the flow in the lower part of the domain becoming very weak.

At higher Da (Da = 10^{-3}) a stronger flow is obtained with its overall structure similar to the one obtained for $Da = 10^{-5}$. The higher strength of the flow is demonstrated by the eye of the recirculating eddy, which is seen to move further downward and upward for negative and positive values of the buoyancy ratio (compare Figures 5g-5i with Figures 5a-5f), respectively. Difference from results obtained for $Da = 10^{-5}$, the main recirculating eddy at a buoyancy ratio with a value of -1 rotates clockwise (compare Figures 5c and 5i). In addition, streamlines in Figure 5c reveal the formation of several smaller recirculating eddies rotating counterclockwise. At N = -1, the upward and downward buoyancy forces are of equal strength, which reduces the buoyancy source term in the Y-momentum equation to simply $(\theta - \sigma)$. Therefore, the sign of the source term depends on the local values of θ and σ . At locations where $\theta > \sigma$, buoyancy is in the aiding mode, and at locations where $\theta < \sigma$, buoyancy is in the opposing mode. Moreover, at higher values of Da the non-Darcian effects increase. The combined influence of these terms results in the flow field displayed in Figure 5i. The recirculating bubbles shown in Figures 5g and 5h can be explained in a similar way.

Plots depicted in Figures 6a–6l are for an enclosure with an $E_{\rm g}$ of value 0.75. As shown, generated flow fields are similar to

heat transfer engineering

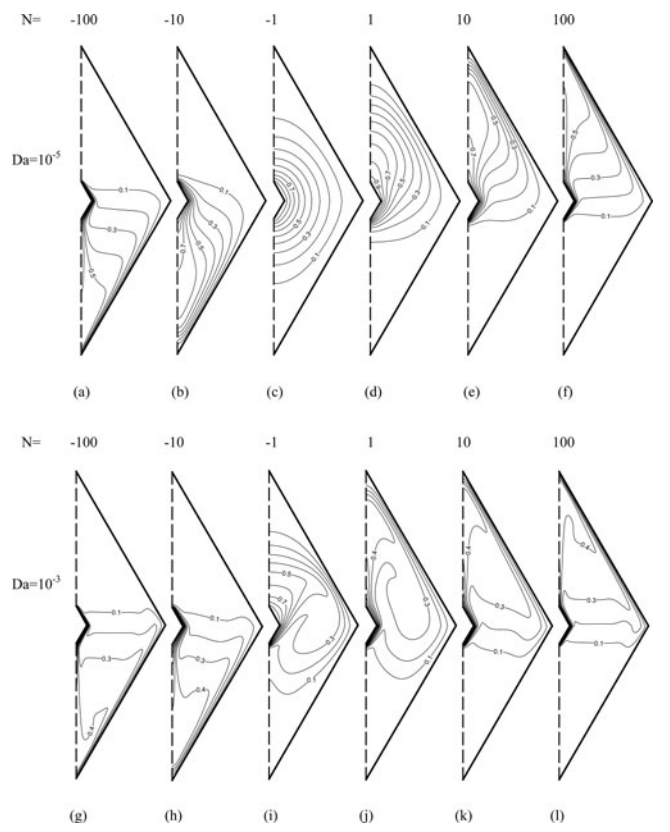


Figure 9 Isoconcentrations for different values of the buoyancy ratio (N) $(E_g=0.875, \epsilon=0.6, Ra=10^6, Pr=0.7).$

those displayed in Figure 5 with the eye of the recirculating eddy, for both values of Da considered, moving upward from the lower half to the upper half of the enclosure as N increases from -100 to 100. At Da $= 10^{-5}$ and N = -1 (Figure 6c), streamline values are of order 10^{-10} , indicating an almost stagnant fluid in the cavity. By comparing streamlines in Figure 6 with corresponding ones in Figure 5 it can be inferred that as Eg decreases, the proportion of the hot to the cold surface area increases, and the stratification effects in the upper half of the domain for negative values of the buoyancy ratio and in the lower half for N > 0 decrease. Moreover, the strength of the flow is slightly lower due to a decrease in the available convective area and due to the greater viscous effects of the added surface area.

Isotherms in the enclosures for which streamlines were reported in Figures 5 and 6 are displayed in Figures 7 and 8, respectively. In Figure 7 ($E_g=0.875$) and at the lowest buoyancy ratio considered (i.e., N=-100), isotherms are concentrated in the lower part of the enclosure (Figures 7a and 7g) because the net buoyancy force is acting downward. A high stratification level characterizes the upper half of the domain. As the buoyancy ratio increases while remaining negative (i.e., N=-10), the concentration of isotherms remains biased toward the lower half of the domain, with this preference being more apparent at the higher value of Da (Da = 10^{-3} , Figure 7h), where a lower stratification level in the upper part of the domain is predicted. At a buoyancy ratio with a value of -1, a uniform distribution

of isotherms is obtained at $Da = 10^{-5}$, indicating a conduction/diffusion dominated heat and mass transfer problem. This distribution of isotherms agrees with the predicted flow field depicted in Figure 5c, which indicated an almost stagnant fluid in the enclosure. At Da = 10^{-3} , isotherms shown in Figure 7i are spread over the domain while being slightly biased toward the upper half for reasons explained earlier. For positive values of the buoyancy ratio (Figures 7e-7f and 7j-7l), except for the case when N = 1 and $Da = 10^{-5}$, the hot fluid is located in the upper part of the enclosure where isotherms are concentrated, with the lower part of the domain being highly stratified. The level of stratification is higher at higher values of N and/or Da. For N = 1 and $Da = 10^{-5}$, the flow is still weak for convection to have noticeable effects, and isotherms are uniformly distributed over the domain, indicating that conduction is still the dominant heat transfer mechanism in the enclosure. The distributions of isotherms presented in Figures 8a–81 for an enclosure gap (E_g) with a value of 0.75 are similar to corresponding ones presented in Figure 7, with the ones displayed in Figure 8 being less dense, indicating weaker flows and consequently lower convection effects. As mentioned earlier, this decrease in convection is due to the lower available flow area and higher viscous effects as a result of the greater hot wall surface area.

The corresponding isoconcentration maps for the cases discussed above are displayed in Figures 9a–9l and 10a–10l. The distribution of isoconcentration lines over the domain at differ-

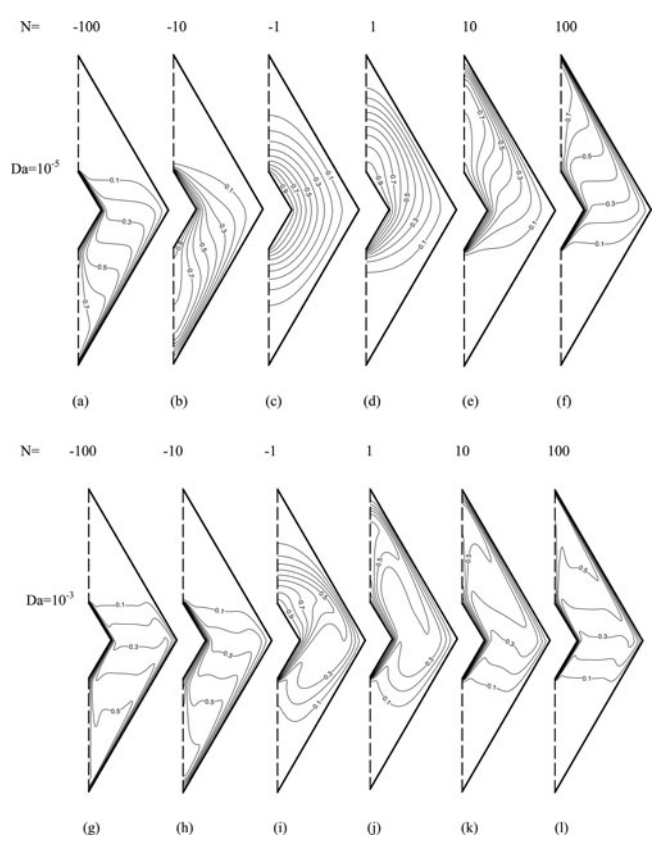


Figure 10 Isoconcentrations for different values of the buoyancy ratio (N) $(E_\sigma=0.75,\,\epsilon=0.6,\,Ra=10^6,\,Pr=0.7).$

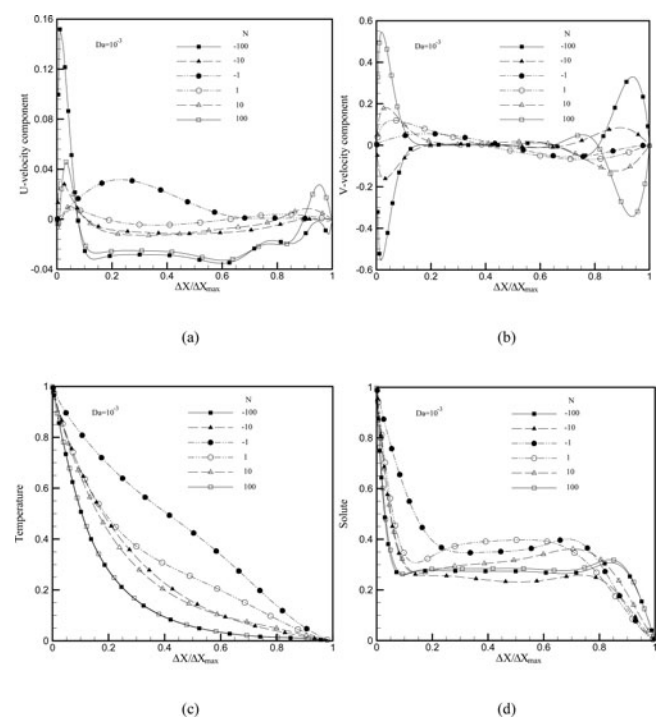


Figure 11 The effect of buoyancy ratio (N) on mid-height (a) X-velocity, (b) Y-velocity, (c) dimensionless temperature, and (d) solute profiles (Ra = 10^6 , $E_g = 0.75$, $\epsilon = 0.6$, Pr = 0.7).

ent values of N and Da is similar to corresponding isotherm maps presented in Figures 7 and 8, with isoconcentrations being more distorted. This higher distortion is due to the lower diffusion coefficient of the solute [Eq. (10)] in comparison with the diffusion coefficient of temperature [Eq. (9)] as the value of Lewis number used in this study is fixed at 10. Due to this fact, convection has a higher influence on solute distribution than on temperature distribution. Furthermore, similar to isotherm maps (Figures 7 and 8), the distributions of isoconcentrations over the domain at given values of Da and E_g are almost symmetric with respect to the horizontal centerline of the rhombic annulus at opposite values of N. This is especially true at high values of N (i.e., $N = \pm 10$ and $N = \pm 100$), where the effects of temperature gradients become negligible in comparison with concentration gradients (e.g., compare Figures 9g and 9l and Figures 10b and 10e).

Velocity, Temperature, and Concentration Profiles

The effects of the buoyancy ratio on the X-velocity component, Y-velocity component, temperature, and concentration profiles along the horizontal centerline of the domain are displayed in Figure 11 for an enclosure with $E_g=0.75$, $Ra_T=10^6$, $Da=10^{-3}$, $\epsilon=0.6$, and Pr=0.7. Variation of the various quantities are plotted in terms of a dimensionless distance $(\Delta X/\Delta X_{max})$ defined as

$$\frac{\Delta X}{\Delta X_{\text{max}}} = \frac{X - X_{\text{min}}}{X_{\text{max}} - X_{\text{min}}}$$
 (17)

Profiles displayed in Figures 11a and 11b indicate that the U-velocity component is an order of magnitude lower than the V-velocity component. This is expected, as buoyancy forces act in the vertical direction and the U-values are mainly dictated by the domain geometry. The boundary-layer behavior is clear near the walls where both the U- and V-velocity components peak. The peaks near the hot wall are much larger than those in the vicinity of the cold wall due to the lower hot wall area. Moreover, these peaks are higher at higher |N| values due to higher buoyancy forces. Furthermore, the sign of the V-velocity profile indicates the direction of the flow. For positive N values, V profiles indicate an upward flow over the hot walls and a downward flow along the cold walls of the enclosure and vice versa. Profiles for $\pm N$ are nearly symmetric with respect to the horizontal centerline of the annulus.

The corresponding temperature and concentration profiles are presented in Figures 11c and 11d, respectively. The increase in convection contribution to total heat transfer at higher values of |N| (Figure 11c) is reflected by the nonlinear temperature distribution along the horizontal centerline of the enclosure. Similar conclusions can be drawn for variation in the concentration profiles with convection effects being more pronounced (Figure 11d) due to the high value of Lewis number (Le = 10). The sharp slopes in the concentration profiles clearly show the boundary-layer behavior close to the enclosure walls, with gradients being steeper at higher |N| values.

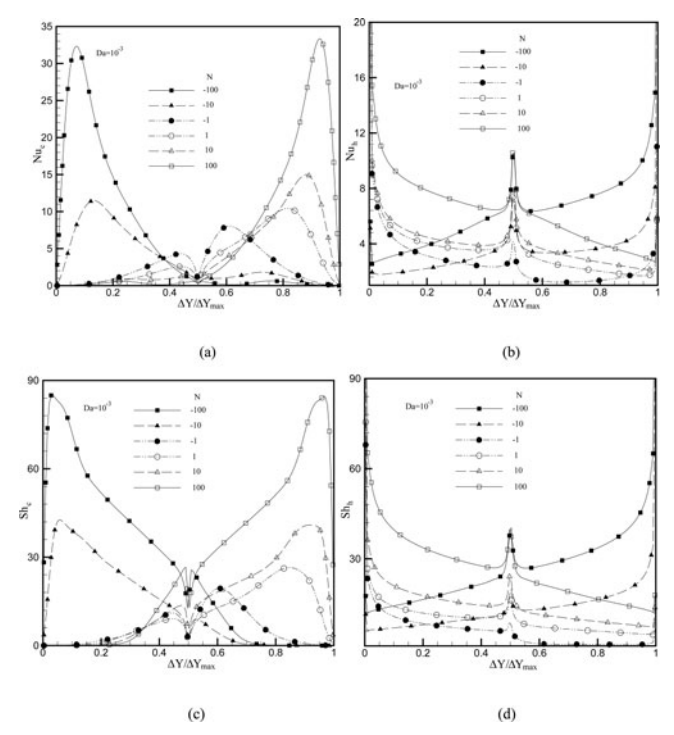


Figure 12 The effect of buoyancy ratio (N) on local Nusselt (a,b) and Sherwood (c,d) number distribution along the cold (a,c) and hot (b,d) walls of the enclosure (Ra = 10^6 , E_g = 0.75, ϵ = 0.6, Pr = 0.7).

Table 2 Average Nusselt number values (\overline{Nu}) for Pr = 0.7 (Le = 10)

$\epsilon = 0.3$			$E_g =$	0.875					$E_g =$	= 0.75				$E_g = 0.5$				
Ra	10)5	10	0^{6}	1	07	10	05	10)6	1	07	10) ⁵	10)6	1	07
N, Da	10^{-5}	10^{-3}	10^{-5}	10^{-3}	10^{-5}	10^{-3}	10^{-5}	10^{-3}	10^{-5}	10^{-3}	10^{-5}	10^{-3}	10^{-5}	10^{-3}	10^{-5}	10^{-3}	10^{-5}	10^{-3}
-100	1.60	2.19	2.50	3.52	4.85	6.31	2.44	3.24	3.56	5.22	6.46	9.50	5.07	5.74	6.02	7.58	8.93	11.98
-10	1.46	1.61	1.58	2.08	2.37	3.22	2.28	2.46	2.42	3.10	3.42	4.81	4.99	5.05	5.06	5.63	5.89	7.26
-1	1.45	1.45	1.45	1.71	1.50	2.78	2.28	2.28	2.28	2.49	2.34	4.23	4.99	4.99	4.99	5.02	5.02	6.13
1	1.45	1.50	1.47	2.18	1.93	3.82	2.28	2.31	2.29	2.99	2.76	5.58	4.99	5.00	5.00	5.20	5.23	7.59
10	1.46	1.68	1.62	2.37	2.70	4.07	2.28	2.52	2.46	3.52	3.77	5.94	4.99	5.07	5.08	5.92	6.20	8.41
100	1.60	2.21	2.54	3.61	5.34	7.15	2.44	3.32	3.60	5.33	6.89	9.73	5.07	5.77	6.05	7.80	9.19	12.26
$\varepsilon = 0.6$			$E_g =$	0.875					$E_g =$	= 0.75					E_{g}	= 0.5		
-100	1.62	2.57	2.79	4.45	5.96	8.24	2.46	3.69	3.90	6.43	7.76	12.18	5.09	6.25	6.32	8.82	10.23	14.68
-10	1.46	1.70	1.60	2.39	2.62	4.04	2.28	2.58	2.44	3.47	3.72	5.77	4.99	5.14	5.07	6.04	6.15	8.15
-1	1.45	1.46	1.45	1.91	1.50	3.34	2.28	2.28	2.28	2.72	2.35	5.30	4.99	4.99	4.99	5.09	5.03	7.36
1	1.45	1.55	1.47	2.62	2.02	4.70	2.28	2.36	2.29	3.59	2.86	6.86	4.99	5.01	5.00	5.52	5.29	9.45
10	1.46	1.82	1.65	2.96	3.14	5.53	2.29	2.70	2.49	4.13	4.25	7.47	4.99	5.17	5.10	6.56	6.56	9.94
100	1.63	2.70	2.93	4.88	6.63	9.47	2.47	3.81	4.02	6.58	8.36	12.51	5.09	6.30	6.36	8.98	10.61	14.92
$\epsilon = 0.9$			$E_g =$	0.875					$E_g =$	= 0.75					$\mathbf{E}_{\mathbf{g}}$	= 0.5		
-100	1.63	2.84	2.93	5.09	6.63	10.85	2.48	3.99	4.06	7.26	8.56	14.00	5.09	6.57	6.47	9.63	11.04	16.45
-10	1.46	1.77	1.61	2.61	2.75	4.87	2.28	2.66	2.45	3.72	3.87	6.45	4.99	5.19	5.08	6.30	6.29	8.80
-1	1.45	1.47	1.45	2.09	1.51	3.95	2.28	2.29	2.28	2.89	2.35	6.06	4.99	4.99	4.99	5.13	5.03	8.38
1	1.45	1.59	1.47	2.89	2.05	5.26	2.28	2.40	2.29	3.99	2.91	7.67	4.99	5.02	5.00	5.81	5.32	10.72
10	1.46	1.91	1.66	3.22	3.20	6.34	2.29	2.82	2.51	4.47	4.36	8.53	4.99	5.27	5.11	6.92	6.74	11.03
100	1.64	2.89	3.10	5.63	7.44	11.04	2.48	4.17	4.21	7.47	9.29	14.41	5.10	6.57	6.57	9.82	11.51	16.81

Nusselt and Sherwood Numbers

The local Nusselt and Sherwood numbers along the inner and outer walls of the porous rhombic annulus are calculated

using Eq. (15), while average values are computed via Eq. (16). The local variations in these numbers are presented in Figure 12 with values plotted as a function of a dimensionless distance

Table 3 Average Nusselt number values (\overline{Nu}) for Pr = 5.0 (Le = 10)

$\varepsilon = 0.3$			$E_g =$	0.875					Eg =	= 0.75					E_g	= 0.5		
Ra	10)5	10)6	1	07	10)5	10)6	1	07	10	05	1	06	10	07
N, Da	10^{-5}	10^{-3}	10^{-5}	10^{-3}	10^{-5}	10^{-3}	10^{-5}	10^{-3}	10^{-5}	10^{-3}	10^{-5}	10^{-3}	10^{-5}	10^{-3}	10^{-5}	10^{-3}	10^{-5}	10^{-3}
-100	1.61	2.40	2.71	4.09	5.91	7.52	2.45	3.48	3.80	5.55	7.69	9.99	5.08	5.92	6.23	8.16	10.13	12.66
-10	1.46	1.63	1.59	2.23	2.54	3.63	2.28	2.49	2.43	3.27	3.62	5.17	4.99	5.06	5.06	5.73	6.06	7.53
-1	1.45	1.45	1.45	1.81	1.50	3.44	2.28	2.28	2.28	2.28	2.35	4.78	4.99	4.99	4.99	5.03	5.02	6.41
1	1.45	1.50	1.47	2.37	1.99	4.30	2.28	2.32	2.29	3.21	2.83	6.30	4.99	5.00	5.00	5.25	5.27	8.54
10	1.46	1.72	1.63	2.70	3.06	4.73	2.28	2.56	2.48	4.04	4.16	6.81	4.99	5.08	5.09	6.10	6.52	9.27
100	1.61	2.44	2.84	4.21	6.57	8.53	2.45	3.54	3.92	5.95	8.31	11.13	5.08	5.96	6.28	8.33	10.55	13.56
$\epsilon = 0.6$	$E_g = 0$).875					$E_g = 0$).75					$E_g = 0$).5				
-100	1.63	2.77	2.92	4.95	6.87	9.24	2.47	3.94	4.05	6.92	8.84	13.18	5.09	6.41	6.46	9.30	11.28	15.73
-10	1.46	1.73	1.61	2.52	2.72	4.36	2.28	2.60	2.45	3.64	3.84	6.08	4.99	5.14	5.08	8.15	6.26	8.43
-1	1.45	1.46	1.45	2.03	1.52	3.91	2.28	2.28	2.28	2.85	2.35	5.42	4.99	4.99	4.99	5.10	5.03	8.18
1	1.45	1.56	1.47	2.80	2.05	5.31	2.28	2.36	2.29	3.84	2.90	7.68	4.99	5.01	5.00	5.61	5.31	10.59
10	1.46	1.87	1.66	3.26	3.32	6.08	2.29	2.75	2.50	4.49	4.45	8.20	4.99	5.19	5.11	6.78	6.79	11.02
100	1.63	2.93	2.96	5.42	7.70	10.56	2.48	4.03	4.18	7.13	9.63	13.58	5.09	6.46	6.55	9.56	11.82	16.46
$\varepsilon = 0.9$	$E_g = 0$).875					$E_g = 0$).75					$E_g = 0$).5				
-100	1.64	3.02	3.02	5.52	7.42	10.41	2.48	4.16	4.19	7.79	9.50	15.16	5.10	6.64	6.58	10.10	11.96	17.78
-10	1.46	1.79	1.61	2.74	2.82	4.86	2.28	2.68	2.46	3.84	3.97	6.81	4.99	5.20	5.08	6.34	6.37	9.05
-1	1.45	1.47	1.45	2.15	1.53	4.85	2.28	2.29	2.28	3.01	2.35	6.51	4.99	4.99	4.99	5.14	5.03	9.08
1	1.45	1.60	1.47	3.06	2.07	5.76	2.28	2.40	2.30	4.23	2.93	8.37	4.99	5.02	5.00	5.92	5.33	11.79
10	1.46	1.96	1.67	3.50	3.32	6.42	2.29	2.87	2.51	4.80	4.50	9.24	4.99	5.29	5.11	7.14	6.88	12.38
100	1.64	3.22	3.21	6.13	8.39	11.99	2.49	4.38	4.34	8.01	10.42	15.37	5.10	6.72	6.69	10.44	12.59	18.81

Table 4 Average Sherwood number values $\overline{(Sh)}$ for Pr = 0.7 (Le = 10)

$\epsilon = 0.3$			E _g =	= 0.875					E_g	= 0.75					E_{g}	= 0.5		
Ra	1	05	1	06	1	07	1	05	1	06	1	07	1	05	1	06	1	07
N, Da	$\overline{10^{-5}}$	10^{-3}	10^{-5}	10^{-3}	10^{-5}	10^{-3}	10^{-5}	10^{-3}	10^{-5}	10^{-3}	10^{-5}	10^{-3}	10^{-5}	10^{-3}	10^{-5}	10^{-3}	10^{-5}	10^{-3}
-100	5.10	7.80	11.73	14.23	23.52	26.72	6.82	11.39	16.27	21.83	32.99	41.99	8.64	15.95	21.51	29.23	43.67	56.09
-10	1.73	4.16	4.87	7.50	11.31	13.66	2.52	5.97	6.51	10.96	15.67	21.12	5.08	7.82	8.28	15.36	20.59	28.74
-1	1.45	1.45	1.45	3.64	2.64	6.92	2.28	2.28	2.28	4.94	4.02	10.60	4.99	4.99	4.99	6.49	6.46	13.03
1	1.47	3.00	2.37	5.89	7.00	10.52	2.29	3.93	3.20	8.27	9.56	15.33	5.00	5.39	5.37	10.88	12.28	21.38
10	1.84	4.51	5.36	8.06	12.22	14.81	2.63	6.47	7.19	12.08	16.97	22.80	5.12	8.42	9.08	16.74	22.55	31.20
100	5.15	7.79	11.85	14.34	25.54	29.6	6.89	11.67	16.44	22.02	34.66	42.17	8.72	16.10	21.71	30.08	44.83	56.46
$\varepsilon = 0.6$	$E_g = 0$	0.875					$E_g = 0$	0.75					$E_g = 0$	0.5				
-100	5.56	9.53	13.89	17.66	29.01	33.60	7.37	13.88	19.10	27.11	40.47	52.99	9.22	19.54	24.84	36.69	53.24	69.90
-10	1.76	4.95	5.30	9.17	13.38	16.96	2.55	7.14	7.02	13.37	18.37	26.00	5.09	9.68	8.80	18.68	23.72	35.04
-1	1.45	1.94	1.45	4.20	2.51	9.07	2.28	2.56	2.28	5.80	4.08	13.38	4.99	4.99	4.99	7.84	6.75	16.78
1	1.47	3.62	2.45	7.12	7.75	14.01	2.29	4.91	3.29	10.09	10.50	19.59	5.00	6.05	5.43	13.70	13.47	26.36
10	1.87	5.39	5.85	10.37	15.11	20.05	2.66	7.77	7.79	14.76	20.36	28.21	5.14	10.55	9.73	20.47	26.11	38.29
100	5.61	9.97	14.59	19.13	31.86	37.97	7.45	14.25	19.66	27.22	42.82	53.25	9.31	19.68	25.08	36.85	54.85	70.47
$\varepsilon = 0.9$	$E_g = 0$	0.875					$E_g = 0$	0.75					$E_g = 0$	0.5				
-100	5.78	10.61	14.97	20.05	32.51	43.75	7.62	15.44	20.47	30.68	45.21	60.52	9.48	21.68	26.50	41.55	59.24	79.53
-10	1.77	5.49	5.51	10.22	14.51	20.93	2.56	7.84	7.25	14.87	19.80	29.43	5.10	10.81	9.03	20.84	25.40	39.67
-1	1.45	2.19	1.45	4.80	2.59	10.84	2.28	2.89	2.28	6.27	4.10	15.30	4.99	4.99	4.99	8.62	6.82	20.02
1	1.47	3.97	2.49	7.91	8.13	14.84	2.30	5.46	3.33	11.23	10.95	21.34	5.00	6.64	5.46	15.35	14.00	29.59
10	1.89	5.93	6.09	11.11	15.65	22.79	2.68	8.59	8.05	16.11	21.44	32.11	5.15	11.85	10.02	22.50	27.97	43.09
100	5.84	10.67	15.91	21.91	35.98	43.83	7.70	16.05	21.28	30.96	48.15	60.88	9.57	21.80	27.16	41.65	61.34	79.78

(18)

 $(\Delta Y/\Delta Y_{\text{max}})$ defined as

$$\frac{\Delta Y}{\Delta Y_{\max}} = \frac{Y - Y_{\min}}{Y_{\max} - Y_{\min}}$$

Local Nusselt number profiles along the cold and hot walls are presented in Figures 12a and 12b, respectively, for an enclosure with $E_g=0.75$, $Ra_T=10^6$, $Da=10^{-3}$, $\varepsilon=0.6$, and Pr=0.7. For positive values of N, results indicate that the Nusselt number peaks on the upper part of the cold wall. This peak is

Table 5 Average Sherwood number values (\overline{Sh}) for Pr = 5.0 (Le = 10)

$\epsilon = 0.3$			Eg =	= 0.875					E_g	= 0.75			$E_g = 0.5$						
Ra	1	05	1	06	1	07	1	.05	1	0^{6}	1	07	1	05	1	$\frac{10^6}{10^{-5} 10^{-3}}$) ⁷	
N, Da	10^{-5}	10^{-3}	10^{-5}	10^{-3}	10^{-5}	10^{-3}	10^{-5}	10^{-3}	10^{-5}	10^{-3}	10^{-5}	10^{-3}	10^{-5}	10^{-3}	10^{-5}	10^{-3}	10^{-5}	10^{-3}	
-100	5.24	8.11	12.69	15.01	26.44	28.71	7.02	12.02	17.72	21.96	37.47	41.61	8.87	16.78	23.36	31.20	50.03	57.00	
-10	1.73	4.27	5.00	7.80	12.21	14.45	2.53	6.18	6.68	11.53	17.01	22.14	5.08	7.98	8.47	15.88	22.27	29.78	
-1	1.45	1.45	1.45	3.92	2.59	8.76	2.28	2.28	2.28	5.39	4.07	11.74	4.99	4.99	4.99	6.72	6.63	14.99	
1	1.47	3.07	2.39	6.16	7.29	11.41	2.29	4.02	3.22	8.66	9.98	16.50	5.00	5.40	5.38	11.34	12.89	22.91	
10	1.84	4.64	5.51	8.43	13.83	15.76	2.63	6.64	7.41	13.78	18.93	24.04	5.12	8.63	9.34	17.36	24.83	32.61	
100	5.29	8.11	13.33	15.14	29.17	32.26	7.09	12.12	18.24	23.09	39.78	45.09	8.95	16.94	23.59	31.41	51.75	59.74	
$\varepsilon = 0.6$			$E_g =$	= 0.875					E_g :	= 0.75					E_g	= 0.5			
-100	5.63	9.67	14.52	18.26	31.62	35.25	7.47	14.47	20.05	27.81	44.53	55.04	9.33	20.11	26.12	38.03	58.93	72.41	
-10	1.76	5.04	5.37	9.31	13.85	17.59	2.55	7.24	7.10	13.89	19.24	26.68	5.09	9.82	8.89	19.21	24.87	36.28	
-1	1.45	1.97	1.45	4.44	2.72	9.78	2.28	2.58	2.28	6.11	4.10	13.27	4.99	4.99	4.99	8.00	6.78	19.87	
1	1.47	3.67	2.46	7.38	7.92	14.76	2.29	4.98	3.30	10.45	10.73	20.67	5.00	6.08	5.44	14.11	13.79	27.98	
10	1.87	5.50	5.93	10.67	15.85	20.83	2.67	7.91	7.90	15.22	21.43	29.24	5.14	10.77	9.86	20.98	9.86	20.98	
100	5.69	10.21	14.53	19.85	35.12	40.10	7.55	14.59	20.63	28.06	47.57	55.47	9.43	20.17	26.57	38.04	61.13	72.73	
$\varepsilon = 0.9$			$E_{g} =$	= 0.875					E_g :	= 0.75					E_{g}	= 0.5			
-100	5.83	10.78	15.45	20.48	34.87	39.74	7.69	15.71	21.35	31.75	48.91	63.14	9.55	21.87	27.61	42.55	64.37	82.19	
-10	1.77	5.57	5.56	10.49	14.86	19.72	2.56	7.98	7.31	15.23	20.47	30.44	5.10	10.97	9.09	21.02	26.28	40.58	
-1	1.45	2.22	1.45	4.72	2.82	12.60	2.28	2.91	2.28	6.50	4.11	16.40	4.99	4.99	4.99	8.97	6.84	21.85	
1	1.47	4.01	2.49	8.15	8.24	15.54	2.30	5.53	3.33	11.57	11.10	22.31	5.00	6.69	5.46	15.72	14.21	30.94	
10	1.89	6.07	6.14	11.37	16.19	21.67	2.68	8.71	8.13	16.44	22.25	33.28	5.15	12.04	10.10	22.97	29.06	44.09	
100	5.89	11.53	16.49	22.69	39.04	45.65	7.77	16.43	22.09	31.91	52.58	63.86	9.65	22.10	28.20	42.86	67.11	82.75	

due to the impingement of the hot fluid leaving the upper part of the hot wall (carried by the clockwise rotating vortex) on the upper part of the cold wall (Figure 12a). The value of this peak is seen to be higher at higher values of N due to higher buoyancy effects. While moving down the cold wall, the flow is not capable of following the contour of the rhombic enclosure, thereby decreasing the rate of heat transfer. This flow hits the lower half of the cold wall, causing a second peak in Nusselt number there. Unlike the first peak, the value of the second peak decreases as N increases due to an increase in the stratification level in the lower half of the enclosure. For negative values of N, the opposite occurs. In this case the vortex flow rotates counterclockwise moving down along the hot wall. The hot fluid leaving the lower part of the hot wall impinges on the lower part of the cold wall causing the Nusselt number to peak (Figure 12a). Again, the value of this peak is seen to be higher at higher values of |N|. While moving up the cold wall, the flow does not follow the contour of the rhombic enclosure (reducing heat transfer), hitting the upper part of the cold wall and causing a second peak in Nusselt number there. Again the value of this peak decreases as the magnitude of N increases due to an increase in the stratification level in the upper half of the enclosure.

Along the hot wall (Figure 12b) the Nusselt number peaks near the bottom region for positive values of N and near the top region for negative values of N. In all cases a sharp peak is obtained at mid-height. In the aiding mode (N > 0), the cooled fluid from the lower part of the cold wall is transported by the clockwise eddy toward the lower part of the hot wall, and the largest temperature gradients and Nusselt numbers therefore occur in the leading region of the hot wall. In the opposing mode (N < 0), the cooled fluid from the upper part of the cold wall is transported by the counterclockwise rotating eddy toward the upper regions of the hot wall, increasing Nu there. The sharp peak at mid-height of the domain is due to the acceleration of the flow until reaching the tip of either the lower part or the upper part of the hot wall where it has to change direction to turn around the corner. Again the level of Nusselt number and the values of the peaks increase as |N| increases.

The Sherwood number profiles along the cold and hot walls of the annulus are depicted in Figures 12c and 12d, respectively. Variations in local Sh values are similar to variations in local Nu values for the same reasons stated above. The only difference between the two sets of profiles is in the level of Sh values, which is much higher than the Nu values due to higher convection effects as a result of the high value of Lewis number (Le = 10).

The average Nu values for all cases studied are presented in Table 2 for Pr=0.7 and Table 3 for Pr=5. At $Ra_T=10^5$ and $Da=10^{-5}$ (Table 2), predictions indicate that diffusion is the dominant heat transfer mode in the enclosure. This is demonstrated by the \overline{Nu} values, which are independent of the enclosure porosity, the buoyancy ratio (except at |N|=100, where convection starts to contribute to total heat transfer), and the Prandtl number. The increase in \overline{Nu} as E_g decreases is due

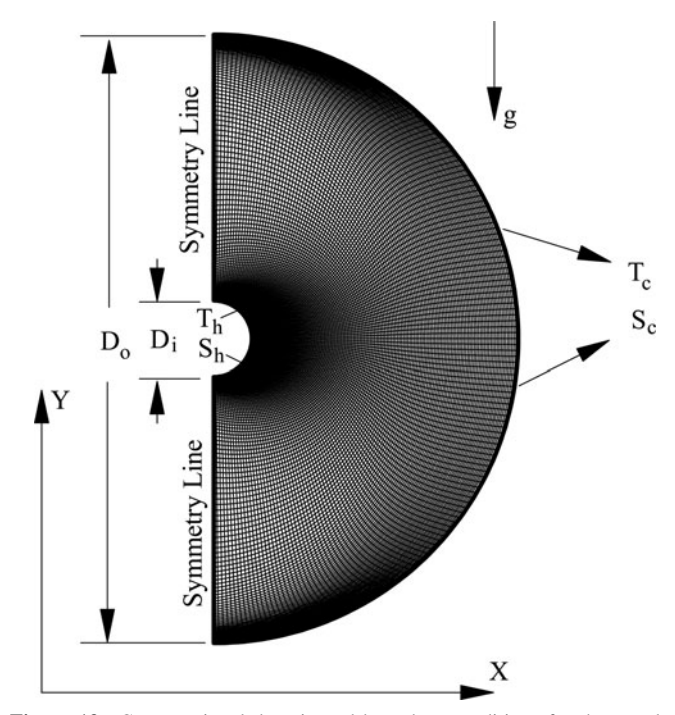


Figure 13 Computational domain and boundary conditions for the annulus between two concentric horizontal circular cylinders.

to an increase in the hot wall area. At other values of Ra_T and/or Da, convection contribution to total heat transfer starts at lower values of the buoyancy ratio, with the value of |N| at which convection begins affecting heat transfer decreasing as ϵ increases. The overall heat transfer (\overline{Nu}) increases with an increase in |N| and/or Ra_T due to stronger buoyancy effects, an increase in ϵ due to an increase in the available convective area

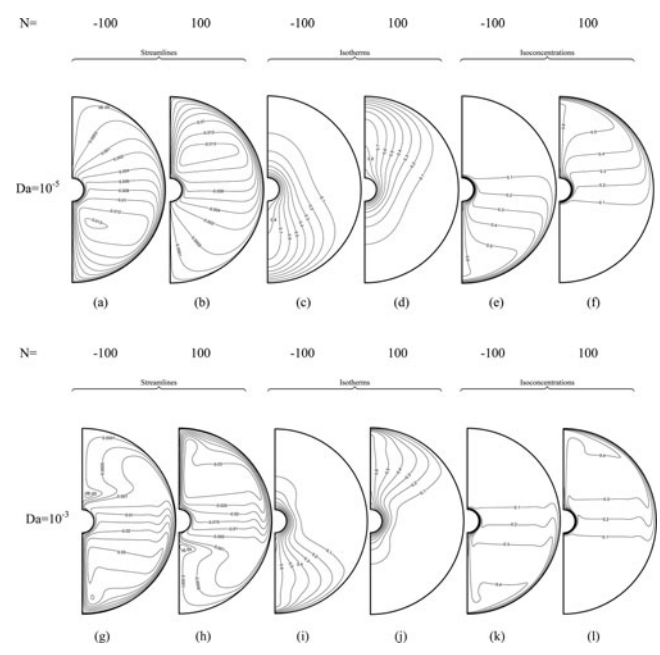


Figure 14 Streamlines, isotherms, and isoconcentrations in the annulus between two horizontal concentric circular cylinders ($\epsilon = 0.6$, Ra = 10^6 , Pr = 0.7).

Table 6 Average Nusselt number values (\overline{Nu}) in a circular annulus for Pr = 0.7 (Le = 10)

$\epsilon = 0.6$				\overline{Nu}					$\%\Delta$	(\overline{Nu})		
Ra	1	.05	1	06	1	07	10	05	10) ⁶	10)7
N, Da	$\overline{10^{-5}}$	10^{-3}	10^{-5}	10^{-3}	10^{-5}	10^{-3}	10^{-5}	10^{-3}	10^{-5}	10^{-3}	10^{-5}	10^{-3}
-100	1.51	2.71	2.75	4.89	6.22	8.99	-7.28	5.17	-1.45	9.00	4.18	8.34
-10	1.32	1.65	1.49	2.47	2.56	4.31	-10.61	-3.03	-7.38	3.24	-2.34	6.26
-1	1.31	1.36	1.31	2.04	1.40	3.93	-10.69	-7.35	-10.69	6.37	-7.14	15.01
1	1.31	1.53	1.34	2.77	2.04	4.87	-10.69	-1.31	-9.70	5.42	0.98	3.49
10	1.32	1.81	1.55	3.06	3.02	5.62	-10.61	-0.55	-6.45	3.27	-3.97	1.60
100	1.52	2.77	2.79	5.02	6.36	9.26	-7.24	2.53	-5.02	2.79	-4.25	-2.27
b Average	Sherwood	number val	ues (\overline{Sh}) in	a circular ar	nnulus for P	r = 0.7 (Le	= 10)					
$\varepsilon = 0.6$				\overline{Sh}					%∆	(Šh)		
-100	5.70	10.35	14.11	19.22	29.66	35.69	2.46	7.92	1.56	8.12	2.19	5.86
-10	1.77	5.35	5.44	9.87	13.57	18.32	0.56	7.48	2.57	7.09	1.40	7.42
-1	1.31	2.41	1.31	4.88	2.61	11.12	-10.69	19.50	-10.69	13.93	3.83	18.44
1	1.34	4.05	2.62	7.90	8.02	14.66	-9.70	10.62	6.49	9.87	3.37	4.43
10	1.93	5.84	6.00	10.82	14.72	20.20	3.11	7.71	2.50	4.16	-2.65	0.74
100	5.75	10.40	14.23	19.40	29.88	36.09	2.43	4.13	-2.53	1.39	-6.63	-5.21

that leads to a lower hydrodynamic resistance, and a decrease in E_g due to an increase in the hot wall area and consequently an increase in conduction contribution to total heat transfer. The highest Nu is obtained at the highest values of Ra_T , N, ε , and E_g . At low values of Ra and ε , estimates at $\pm N$ are nearly equal, with values at positive N being slightly higher as buoyancy forces resulting from temperature and concentration gradients are both in the upward direction. As Ra_T and ϵ increase, the difference between the \overline{Nu} values obtained at $\pm N$ increases. The largest difference in values is obtained in an enclosure with the highest E_g value, that is, the largest convective area. At Pr =5 (Table 3), the predicted \overline{Nu} values are equal to those obtained for Pr = 0.7 for the cases when conduction is the dominant heat transfer mode. When convection effects are important (i.e., at high Ra_T and/or Da values), higher \overline{Nu} are obtained at higher Pr, indicating higher heat transfer rates. This increase in heat transfer is due to a decrease in the thermal boundary layer, which results in higher temperature gradients. The highest \overline{Nu} value of 18.81 is found for the lowest Eg, and the highest Da, Ra_T, Pr, N, and ε. Furthermore, when conduction is the dominant heat transfer mode, \overline{Nu} predictions depend only on E_g.

The \overline{Sh} values are presented in Tables 4 and 5 for Pr = 0.7 and 5, respectively. Predictions indicate that for all values of Ra_T and Da considered, mass transfer increases as the magnitude of the buoyancy ratio increases. Moreover, for different enclosure gap and porosity values, convection contribution to mass transfer starts at values of N lower than the values for which convection starts impacting total heat transfer due to the high Lewis number value used (i.e., Le = 10), which results in a high convection mass transfer coefficient. For diffusion-dominated mass transfer mode (i.e., $N = \pm 1$), predictions indicate that \overline{Sh} and \overline{Nu} values are equal. At higher N values, \overline{Sh} predictions are higher than \overline{Nu} estimates, with the difference increasing as N increases due to the higher convection mass transfer coefficient in comparison

with the convection heat transfer coefficient, as explained earlier. The effects of the enclosure gap and Pr number (Table 5) on the variation of \overline{Sh} is similar to their effects on \overline{Nu} , which was described earlier and is deemed unnecessary to be repeated.

COMPARISON WITH RESULTS IN A CIRCULAR ANNULUS

It is interesting to quantitatively compare the heat and mass transfer obtained in the rhombic annulus with values obtained in a circular annulus between two concentric horizontal cylinders for the same inner and outer perimeters. For that purpose, a rhombic annulus with an E_g value of 0.875 is selected. The equivalent circular annulus is obtained with two horizonal concentric pipes of inner (D_i) and outer (D_o) diameters of size nearly equal to $D_i = 0.0919$ and $D_o = 0.7351$, respectively, resulting in the same inner and outer perimeters as the rhombic annulus. The physical situation and boundary conditions considered are displayed in Figure 13. Results in the enclosure are generated for a total of 36 cases with the values of ε , Le, and Pr fixed at 0.6, 10, and 0.7, respectively. The problem is solved, subject to the same boundary conditions given by Eqs. (11)–(13), for three values of $Ra_T (10^5, 10^6, and 10^7)$, two values of Da $(10^{-5} and 10^{-3})$, and six values of N (-100, -10, -1, 1, 10, and 100). Representative streamlines, isotherms, and isoconcentrations are displayed in Figure 14 for values of N equal to -100 and 100. The trend of results is similar to that reported for the rhombic enclosure with streamlines presented in Figures 14a, 14b, 14g, and 14h, being similar to corresponding cases presented in Figures 5a, 5f, 5g, and 51, respectively. For N = -100 the strongest eddies are located in the lower half of the domain, while the opposite is true for N = 100. Stronger flow is predicted at the higher value of Da. Similar to contours displayed in Figures 7a, 7f, 7g, and 7l, isotherms depicted in Figures 14c, 14d, 14i, and 14j are concentrated in the lower half of the domain for N=-100 and in the upper half for N=100. The same is true for isoconcentrations shown in Figures 14e, 14f, 14k, and 14l, which indicate, similar to lines reported in Figures 9a, 9f, 9g, and 9l, a stratification in the upper half of the domain for N=-100 and in the lower half for N=100. In all cases the stratification is higher at the higher value of Da.

The average Nusselt and Sherwood numbers in the enclosure for the various cases are depicted in Tables 6a and 6b, respectively. In addition to \overline{Nu} and \overline{Sh} values, the tables also display the percent differences between the current values and the corresponding values obtained in a rhombic annulus. These values are computed as

$$\%\Delta\left(\overline{Nu}\right) = 100 * \frac{\left(\overline{Nu}_{\text{circular}} - \overline{Nu}_{\text{Rhombic}}\right)}{\overline{Nu}_{\text{circular}}}$$

$$\% \Delta \left(\overline{Sh} \right) = 100 * \frac{\left(\overline{Sh}_{\text{circular}} - \overline{Sh}_{\text{Rhombic}} \right)}{\overline{Sh}_{\text{circular}}}$$
(19)

As shown in Table 6a, the $\%\Delta(\overline{Nu})$ varies between -10.69% and 15.01%. Similarly, the $\%\Delta(\overline{Sh})$ values displayed in Table 6b indicate variations between -10.69% and 19.50%. These differences in values do not seem to follow a clear trend. Therefore, a large error will be committed if heat and mass transfer in complex geometries is evaluated by just exploiting corresponding values obtained in circular geometries, and this justifies the need for conducting the current study.

CLOSING REMARKS

The effect of buoyancy ratio due to both heat and mass transfer on natural convection in a porous enclosure of rhombic cross section was studied numerically using a finite-volume method. Solutions were generated for several values of thermal Rayleigh number (Ra_T), Darcy number (Da), Prandtl number (Pr), porosity (ϵ), enclosure gap (E_g), and buoyancy ratio (N) in the opposing (N < 0) and aiding mode (N > 0), for a fixed value of Lewis number (Le = 10). It was found that the strength of the flow increases as the |N| increases. Results also showed that \overline{Nu} and \overline{Sh} values increase as the buoyancy ratio increases in either the aiding or the opposing mode, with values obtained in the aiding mode being higher than corresponding values obtained in the opposing mode. The difference decreases as |N| increases. Comparison of average Nusselt and Sherwood number values obtained in the rhombic annulus with similar ones obtained in a circular annulus having the same inner and outer perimeters as the rhombic enclosure, indicated large percent difference in values, thereby justifying the need to study the rhombic geometry.

heat transfer engineering

FUNDING

The financial support provided by the University Research Board of the American University of Beirut is gratefully acknowledged.

NOMENCLATURE

A wall area

 c_p specific heat at constant pressure

 d_p pores diameter

D mass diffusion coefficient

 D_i length of inner pipe's main diagonal

 D_o length of outer pipe's main diagonal

Da Darcy number

 E_g enclosure gap ratio $(E_g = 1 - D_i/D_o)$

F constant in Forchheimer's extension

g gravitational acceleration

k fluid thermal conductivity

K permeability of the porous media

Le Lewis number

n unit vector normal to surface

N buoyancy ratio

Nu local Nusselt number

 \overline{Nu} average Nusselt number

p dimensional pressure

P dimensionless pressure

Pr Prandtl number

Ra Rayleigh number

S dimensional solute concentration

Sh local Sherwood number

 \overline{Sh} average Sherwood number

T dimensional temperature

u, U dimensional and dimensionless x-velocity component

v, V dimensional and dimensionless y-velocity component

x, y dimensional coordinates

X, Y dimensionless coordinates

Greek Symbols

α thermal diffusivity

β volumetric expansion coefficient

ε porosity

θ dimensionless temperature

μ dynamic viscosity

ρ density

σ dimensionless solute concentration

ψ stream function

 Ω rhombus angle

Subscripts

c cold wall or convection heat transfer

h hot wall

- i condition at inner pipe
- o condition at outer pipe
- S refers to concentration
- T refers to temperature
- ∞ refers to a reference value

REFERENCES

- [1] Nishimura, T., Imoto, T., and Miyashita, H., Occurrence and Development of Double-Diffusive Convection During Solidification of a Binary System, *International Journal of Heat and Mass Transfer*, vol. 37, pp. 1455–1464, 1994.
- [2] Makham, B. I., and Rosenberger, F., Diffusive Convection Vapor Transport Across Horizontal and Inclined Rectangular Enclosures, *Journal of Crystal Growth*, vol. 67, pp. 241–254, 1984.
- [3] Bergman, T. L., Incropera, F. P., and Viskanta, R., Correlation of Mixed Layer Growth in a Double-Diffusive, Salt-Stratified System Heated From Below, *Journal of Heat Transfer*, vol. 108, pp. 206–211, 1986.
- [4] Carlsson, J.-O., Processes in Interfacial Zones During Chemical Vapor Deposition: Aspects of Kinetics, Mechanisms, Adhesion and Substrate Atom Transport, *Thin Solid Films*, vol. 130, pp. 261–282, 1985.
- [5] Moukalled, F., and Darwish, M., Double Diffusive Natural Convection in a Porous Rhombic Annulus, *Numerical Heat Transfer, Part A: Applications*, vol. 64, no. 5, pp. 378–399, 2013.
- [6] Nithiarasu, P., Seetharamu, K. N., and Sundararajan, T., Double-Diffusive Natural Convection in an Enclosure Filled With Fluid-Saturated Porous Medium: A Generalized Non-Darcy Approach, *Numerical Heat Transfer, Part A: Applications*, vol. 30, no. 4, pp. 413–426, 1996.
- [7] Borjini, M. N., Kolsi, L., Daous, N., and Ben Aissia, H., Hydromagnetic Double-Diffusive Laminar Natural Convection in a Radiatively Participating Fluid, *Numerical Heat Transfer, Part A: Applications*, vol. 48, no. 5, pp. 483–506, 2005.
- [8] Nishimura, T., Kunitsugu, K., and Morega, A. M., Direct Numerical Simulation of Layer Merging in a Salt-Stratified System, *Numerical Heat Transfer, Part A: Applications*, vol. 37, no. 4, pp. 323–341, 2000.
- [9] Mansour, A., Amahmid, A., Hasnaoui, M., and Bourich, M., Multiplicity of Solutions Induced by Thermosolutal Convection in a Square Porous Cavity Heated From Below and Submitted to Horizontal Concentration Gradient in the Presence of Soret Effect, *Numerical Heat Transfer, Part A:* Applications, vol. 49, no. 1, pp. 69–94, 2006.
- [10] Ghorayeb, K., Khallouf, H., and Mojtabi, A., Onset of Oscillatory Flows in Double-Diffusive Convection, *International Journal of Heat and Mass Transfer*, vol. 42, no. 4, pp. 629–643, 1999.
- [11] Wang, S.Y., Lin, C.X., and Ebadian, M.A., Study of Double-Diffusive Velocity During the Solidification Pro-

- cess Using Particle Image Velocimetry, *International Journal of Heat and Mass Transfer*, vol. 42, no. 24, pp. 4427–4445, 1999.
- [12] Costa, V. A. F., Double Diffusive Natural Convection in a Square Enclosure With Heat and Mass Diffusive Walls, *International Journal of Heat and Mass Transfer*, vol. 40, no. 17, pp. 4061–4071, 1997.
- [13] Chen, Y.-M., and Liou, Ji.-K., Time-Dependent Double-Diffusive Convection due to Salt-Stratified Fluid Layer With Differential Heating in an Inclined Cavity, *International Journal of Heat and Mass Transfer*, vol. 40, no. 3, pp. 711–725, 1997.
- [14] Li, Y.-S., Zhan, J.-M., and Luo, Y.-Y., Unsteady Phenomena In The Double-Diffusive Convection Flows at High Rayleigh Number, *Numerical Heat Transfer, Part A: Applications*, vol. 54, no. 11, pp. 1061–1083, 2008.
- [15] Tanny, J., and Yakubov, B., Experimental Study of a Double-Diffusive Two-Layer System in a Laterally Heated Enclosure, *International Journal of Heat and Mass Transfer*, vol. 42, no. 19, pp. 3619–3629, 1999.
- [16] Tanny, J., Dviri, R., Svizher, A., and Cohen, J., The Structure of a double-Diffusive Interface in a Laterally Heated Enclosure, *International Journal of Heat and Mass Transfer*, vol. 48, no. 23–24, pp. 4926–4941, 2005.
- [17] Lee, J., Kang, S. H., and Son, Y. S., Numerical Study of Multilayered Flow Regime in Double-Diffusive Convection in a Rotating Annulus With Lateral Heating, *Numeri*cal Heat Transfer, Part A: Applications, vol. 38, no, 5, pp. 467–489, 2000.
- [18] Shi, K., and Lu, W.-Q., Time Evolution of Double-Diffusive Convection in a Vertical Cylinder With Radial Temperature and Axial Solutal Gradients, *International Journal of Heat and Mass Transfer*, vol. 49, no. 5–6, pp. 995–1003, 2006.
- [19] Lee, J., Kang, S. H., and Son, Y. S., Experimental Study of Double-Diffusive Convection in a Rotating Annulus With Lateral Heating, *International Journal of Heat and Mass Transfer*, vol. 42, no. 5, pp. 821–832, 1999.
- [20] Kumar, B. V. R., Singh, P., and Bansod, V. J., Effect of Thermal Stratification on Double-Diffusive Natural Convection in a Vertical Porous Enclosure, *Numerical Heat Transfer, Part A: Applications*, vol. 41, no. 4, pp. 421–447, 2002.
- [21] Saghir, M. Z., and Islam, M. R., Double Diffusive Convection in Dual-Permeability, Dual-Porosity Porous Media, *International Journal of Heat and Mass Transfer*, vol. 42, no. 3, pp. 437–454, 1999.
- [22] Malashetty, M. S. and Basavaraja, D., Effect of Time-Periodic Boundary Temperatures on the Onset of Double-Diffusive Convection in a Horizontal Anisotropic Porous Layer, *International Journal of Heat and Mass Transfer*, vol. 47, no. 10–11, pp. 2317–2327, 2004.
- [23] Chamkha, A. J., Double Diffusive Convection in a Porous Enclosure With Cooperating Temperature and Concentra-

- tion Gradients and Heat Generation or Absorption Effects, *Numerical Heat Transfer, Part A: Applications*, vol. 41, no. 1, pp. 65–87, 2002.
- [24] Capone, F., Gentile, M., and Hill, A. A., Double-Diffusive Penetrative Convection Simulated via Internal Heating in an Anisotropic Porous Layer With Throughflow, *International Journal of Heat and Mass Transfer*, vol. 54, no. 7–8, pp. 1622–1626, 2011.
- [25] Karimi-Fard, M., Charrier-Mojtabi, M. C., and Vafai, K., Non-Darcian Effects on Double Diffusive Convection Within a Porous Medium, *Numerical Heat Transfer, Part A: Applications*, vol. 31, no. 8, pp. 837–852, 1997.
- [26] Bennacer, R., Beji, H., Oueslati, F., and Belghith, A., Multiple Natural Convection Solution in Porous Media Under Cross Temperature and Concentration Gradients, *Numerical Heat Transfer, Part A: Applications*, vol. 39, no. 6, pp. 553–567, 2001.
- [27] Bera, P., and Khalili, A., Double-Diffusive Natural Convection in an Anisotropic Porous Cavity With Opposing Buoyancy Forces: Multi-Solutions and Oscillations, *International Journal of Heat and Mass Transfer*, vol. 45, no. 15, pp. 3205–3222, 2002.
- [28] Beji, H., Bennacer, R., Duval, R., and Vasseur, P., Double Diffusive Natural Convection in a Vertical Porous Annulus, *Numerical Heat Transfer, Part A: Applications*, vol. 36, no. 2, pp. 153–170, 1999.
- [29] Costa, V. A. F., Double Diffusive Natural Convection in Parallelogrammic Enclosures Filled With Fluid-Saturated Porous Media, *International Journal of Heat and Mass Transfer*, vol. 47, no. 12–13, pp. 2699–2714, 2004.
- [30] Costa, V. A. F., Double Diffusive Natural Convection in Parallelogrammic Enclosures, *International Journal* of Heat and Mass Transfer, vol. 47, no. 14–16, pp. 2913–2926, 2004.
- [31] Moukalled, F., and Darwish, M., Natural Convection Heat Transfer in a Porous Rhombic Annulus, *Numerical Heat Transfer, Part A: Applications*, vol. 58, no. 1, pp. 101–124, 2010.
- [32] Vafai, K., and Tien, C. L., Boundary and Inertia Effects on Flow and Heat Transfer in Porous Media, *International Journal of Heat and Mass Transfer*, vol. 24, pp. 195–203, 1981.
- [33] Chen, X. B., Yu, P., Winoto, S. H., and Low, H. T., Free Convection in a Porous Wavy Cavity Based on the Darcy–Brinkman–Forchheimer Extended Model, *Numerical Heat Transfer, Part A*, vol. 52, pp. 377–397, 2007.
- [34] Brinkman, H.C., On the Permeability of Media Consisting of Closely Packed Porous Particles, *Applied Science Research*, vol. 1, pp. 81–86, 1947.
- [35] Amiri, A., and Vafai, K., Analysis of Dispersion Effect and Non-Thermal Equilibrium, Non-Darcian Variable Porosity Incompressible Flow through Porous Media, *International Journal of Heat and Mass Transfer*, vol. 37, pp. 939–954, 1994.

- [36] Zwart, P. J., Raithby, G. D., and Raw, M. J., An Integrated Space-Time Finite-Volume Method for Moving-Boundary Problems, *Numerical Heat Transfer, Part B*, vol. 34, pp. 257–270, 1998.
- [37] Gaskell, P. H., and Lau, A. K. C., Curvature Compensated Convective Transport: SMART, a New Boundedness Preserving Transport Algorithm, *International Journal for Numerical Methods in Fluids*, vol. 8, pp. 617–641, 1988.
- [38] Darwish, M., and Moukalled, F., Normalized Variable and Space Formulation Methodology for High-Resolution Schemes, *Numerical Heat Transfer, Part B*, vol. 26, pp. 79–96, 1994.
- [39] Patankar, S. V., *Numerical Heat Transfer and Fluid Flow*, Hemisphere, New York, NY, 1980.
- [40] Moukalled, F., and Darwish, M., Pressure Based Algorithms for Single and Multifluid Flow, in *Handbook of Numerical Heat Transfer*, 2nd edition, eds. W. J. Minkowycz, E. M. Sparrow, and J. Y. Murthy, Wiley, Hoboken, NJ, pp. 325–367, 2006.
- [41] Moukalled, F., and Darwish, M., A Unified Formulation of the Segregated Class of Algorithms for Fluid Flow at All Speeds, *Numerical Heat Transfer, Part B*, vol. 37, no. 1, pp. 103–139, 2000.
- [42] Peric, M., A Finite Volume Method for the Prediction of Three Dimensional Fluid Flow in Complex Ducts, Ph.D. Thesis, Imperial College, Mechanical Engineering Department, London, UK, 1985.
- [43] Goyeau, B., Songbe, J.-P., and Gobin, D., Numerical Study of Double-Diffusive Natural Convection in Porous Cavity Using the Darcy–Brinkman Formulation, *Interna*tional Journal of Heat and Mass Transfer, vol. 39, pp. 1363–1378, 1996.
- [44] Trevisan, O. V., and Bejan, A., Natural Convection With Combined Heat and Mass Transfer Buoyancy Effects in a Porous Medium, *International Journal of Heat and Mass Transfer*, vol. 28, pp. 1597–1611, 1985.



Fadl Moukalled is a professor of mechanical engineering at the American University of Beirut, Lebanon. He received his Ph.D. in 1987 from Louisiana State University, Baton Rouge, LA. His main research interests are computational fluid dynamics, numerical heat transfer, and finite-time thermodynamics.



Marwan Darwish is currently a professor in the Mechanical Engineering Department of the American University of Beirut, Lebanon. His research interest is in computational fluid dynamics, where he has worked on the development of high-resolution schemes, and in the development of pressure–velocity coupling algorithms for all-speed and multifluid flows.